Numerical simulation of vortex shedding flows past moving obstacles using the k-ε turbulence model on unstructured dynamic meshes

Hai Tran — Bruno Koobus — Charbel Farhat

Department of Aerospace Engineering Sciences and
Center for Aerospace Structures
University of Colorado, Campus Box 429
Boulder, CO 80309-0429, USA

ABSTRACT. *We consider the numerical solution on unstructured dynamic meshes of the averaged Navier-Stockes equations equipped with the k-ε turbulence model and a wall function. We discuss discretization issues pertaining to moving grids and numerical dissipation, and present a robust spring analogy method for constructing dynamic meshes. We validate our implementation of this two-equation turbulence model and justify its usage for a class of vortex shedding problems by correlating our computational results with experimental data obtained for a flow past a square cylinder. We also apply our solution methodology to the two-dimensional aerodynamic stability analysis of the Tacoma Narrows Bridge, and report numerical results that are in good agreement with observed data.*

RÉSUMÉ. *On considère la résolution numérique sur maillages mobiles non structurés des équations de Navier-Stockes moyennées équipées d'un modèle de turbulence k-ε avec loi de paroi. Les problèmes de discrétisation associés aux maillages mobiles et à la dissipation numérique sont examinés, et on présente une méthode de mouvement de maillages robuste fondée sur une analogie avec des ressorts. On valide notre implémentation de ce modèle de turbulence à deux équations et justifie son utilisation pour la simulation d'écoulements avec développement de tourbillons en corrélant nos résultats numériques avec des données expérimentales pour un écoulement autour d'un cylindre de section carrée. On applique également notre méthodologie à l'analyse bi-dimensionnelle de la stabilité aérodynamique du pont de Tacoma Narrows ; de bonnes comparaisons entre les résultats numériques et les données observées sont obtenues.*

MOTS-CLÉS : *méthode éléments finis/volumes finis, maillages dynamiques, modèle de turbulence k-ε, écoulements avec tourbillons.*

KEY WORDS : *finite element/finite volume method, dynamix meshes, k-ε turbulence model, vortex shedding flows.*

Revue européenne des éléments finis. Volume 6 - n°5-6/1997, pages 611 à 642

1. Introduction

The numerical simulation of vortex shedding flows past oscillating obstacles is important for many engineering applications, including the buffeting analysis of aircraft [1], and the aerodynamic stability analysis of suspension bridges [2, 3]. It requires the solution of the Navier-Stokes equations on moving and possibly deforming grids. Direct numerical simulations (DNS) have made significant progress in recent years, as three-dimensional vortex shedding computations with Reynolds numbers as large as $Re = 5000$ are now possible on large-scale massively parallel processors [4]. However, even though they are not perfect, turbulence models are still widely used for the simulation of viscous flow problems at higher Reynolds numbers, or when the computational resources required by DNS methods are not available.

Whether DNS or large eddy simulations (LES) are preferred, or only a turbulence model can be afforded, the solution of the governing Navier-Stokes equations on unstructured moving and deforming grids calls for careful spatial and temporal discretization methods, and a robust strategy for constructing dynamic meshes. Here, our main objectives are (a) to present a solution methodology for the simulation of vortex dominated flow problems past moving bodies, and (b) to illustrate this methodology with the aeroelastic stability analysis of a suspension bridge. For practical purposes, we consider the k-ε turbulence model, but many of the algorithmic issues we discuss in this paper equally apply to other turbulence models, as well as to DNS and LES methods. The remainder of this paper is organized as follows.

In Section 2 we formulate the averaged compressible Navier-Stokes equations augmented with the k-ε turbulence model [5] in arbitrary Lagrangian Eulerian (ALE) form [6]. In Section 3, we overview the second-order semidiscretization of these equations by a combination of unstructured finite volumes and finite elements. In Section 4, we discuss the time-integration of the resulting semidiscrete convective and diffusive fluxes on unstructured moving grids, and emphasize conservation and accuracy issues. In Section 5, we overview the solution of the resulting system of nonlinear equations. In Section 6, we describe a robust spring analogy method for constructing dynamic viscous fluid meshes that deform to follow the computational domain geometries. In Section 7, we consider a flow past a square cylinder. We validate our implementation and justify the suitability of the k-ε turbulence model with a wall function for vortex shedding problems by correlating our computational results with the available experimental data. In particular, we revisit the conclusions formulated in [7], and show that for the square cylinder problem, the k-ε turbulence model is capable of reproducing the correct Strouhal number as well as the correct time-averaged drag coefficient, when the numerical dissipation induced by upwinding is properly controlled. In Section 8 we apply our computational methodology to the two-dimensional aerodynamic stability analysis of the Tacoma Narrows Bridge, and predict a critical wind speed that is within 23% of the estimated real value. Finally, in Section 9 we conclude this paper and comment on the performance of the k-ε turbulence model as employed and discretized in this paper.

2. Governing equations

In the simulation of flow problems with moving boundaries, a body-conforming mesh has to be regenerated at each time-step, or the existing grid has to be allowed to deform to follow the computational domain geometries. The former option is rather cumbersome and computationally expensive, especially for three-dimensional problems. The latter option introduces the concept of a moving and deforming unstructured grid that is usually referred to as a "dynamic mesh".

Several approaches exist for solving flow problems on dynamic meshes, among which we note ALE methods [6, 8] and space-time formulations [9, 10]. In this paper, we adopt the ALE approach because of its immense popularity for the solution of fluid/structure interaction problems, especially in the aeronautics community.

2.1. *ALE form of the averaged Navier-Stokes equations*

Let $\mathcal{D}(t)$ be the flow domain of interest, and $\Gamma(t)$ be its moving and/or deforming boundary. We introduce a mapping function between $\mathcal{D}(t)$ where time is denoted by t and a grid point's coordinates by x, and a reference configuration $\mathcal{D}(0)$ where time is denoted by Θ and a grid point's coordinates by ξ, as follows

$$x = x(\xi,\Theta); \quad t=\Theta \tag{1}$$

The ALE nondimensional conservative form of the averaged Navier-Stokes equations describing viscous flows on dynamic meshes can be written as [8]

$$\frac{\partial JW}{\partial t}|_\xi + J\nabla_x.\mathcal{F}^c(W,\dot{x}) = J\nabla_x.\mathcal{R}(W) \tag{2}$$

$$\mathcal{F}^c(W,\dot{x}) = \mathcal{F}(W) - \dot{x}W$$

where a dot superscript designates a time derivative, $J = det(dx/d\xi)$, $\dot{x} = \frac{\partial x}{\partial \Theta}|_\xi$, W is the fluid state vector, $\mathcal{F}^c$ denotes the ALE convective fluxes, and $\mathcal{R}$ the diffusive fluxes.

For two-dimensional flows, W, $\mathcal{F}$ and $\mathcal{R}$ are given by

$$W = \begin{pmatrix} \rho \\ \rho v_1 \\ \rho v_2 \\ E \end{pmatrix}$$

$$\mathcal{F}(W)=\begin{pmatrix}\mathcal{F}_1(W)\\ \mathcal{F}_2(W)\end{pmatrix}\quad,\quad \mathcal{R}(W)=\begin{pmatrix}\mathcal{R}_1(W)\\ \mathcal{R}_2(W)\end{pmatrix}$$

where

$$\mathcal{F}_1(W)=\begin{pmatrix}\rho v_1\\ \rho v_1^2+p\\ \rho v_1 v_2\\ (E+p)\,v_1\end{pmatrix}\quad,\quad \mathcal{F}_2(W)=\begin{pmatrix}\rho v_2\\ \rho v_1 v_2\\ \rho v_2^2+p\\ (E+p)\,v_2\end{pmatrix}$$

$$\mathcal{R}_1(W)=$$

$$\frac{\mu}{Re}\begin{pmatrix}0\\ \sigma_{11}\\ \sigma_{12}\\ v_1\sigma_{11}+v_2\sigma_{12}+\dfrac{\gamma}{Pr}\dfrac{\partial e}{\partial x_1}\end{pmatrix}+\frac{1}{R_t}\begin{pmatrix}0\\ \sigma_{11}-\dfrac{2}{3}\rho k R_t\\ \sigma_{12}\\ v_1\sigma_{11}+v_2\sigma_{12}-\dfrac{2}{3}\rho k v_1 R_t+\dfrac{\gamma}{Pr_t}\dfrac{\partial e}{\partial x_1}\end{pmatrix}$$

$$\mathcal{R}_2(W)=$$

$$\frac{\mu}{Re}\begin{pmatrix}0\\ \sigma_{12}\\ \sigma_{22}\\ v_1\sigma_{12}+v_2\sigma_{22}+\dfrac{\gamma}{Pr}\dfrac{\partial e}{\partial x_2}\end{pmatrix}+\frac{1}{R_t}\begin{pmatrix}0\\ \sigma_{12}\\ \sigma_{22}-\frac{2}{3}\rho k R_t\\ v_1\sigma_{12}+v_2\sigma_{22}-\dfrac{2}{3}\rho k v_2 R_t+\dfrac{\gamma}{Pr_t}\dfrac{\partial e}{\partial x_2}\end{pmatrix}$$

$$\begin{aligned}
E &= \rho e+\tfrac{1}{2}\rho\|v\|^2+\rho k\\
v &= (v_1,v_2)^T\\
p &= (\gamma-1)\rho e\\
\sigma &= \nabla v+\nabla^T v-\frac{2}{3}\nabla .v I_d\\
\gamma &= \frac{c_p}{c_v}
\end{aligned}$$

and ρ is the fluid density, p its pressure, e its specific internal energy, v its velocity vector, μ its molecular viscosity, γ its specific heat ratio, Re and Re_t are the laminar and turbulent Reynolds numbers, respectively, Pr and Pr_t are the laminar and turbulent Prandtl numbers, σ the stress tensor, k the kinetic energy of turbulence, I_d the identity matrix, and a T superscript designates the transpose of a vector.

The extension of the expressions of W, $\mathcal{F}$ and $\mathcal{R}$ to three-dimensional flows is straightforward.

2.2. *Two-equation $k-\varepsilon$ turbulence model*

The closure of system (2) is performed here by a two-equation high Reynolds $k-\varepsilon$ model. Using the subscript t for designating a turbulent variable, the equations governing this turbulence model can be written in ALE form as follows

$$\frac{\partial J W_t}{\partial t}|_\xi + J\nabla_x.\mathcal{F}_t^c(W_t,\dot{x}) = J\nabla_x.\mathcal{R}_t(W_t) + J\Omega(W_t) \tag{3}$$

$$\mathcal{F}_t^c(W_t,\dot{x}) = \mathcal{F}_t(W_t) - \dot{x}W_t$$

$$W_t = \begin{pmatrix} \rho k \\ \rho \varepsilon \end{pmatrix}$$

For two-dimensional flows, $\mathcal{F}_t(W_t)$ and $\mathcal{R}_t(W_t)$ can be expressed as

$$\mathcal{F}_t(W_t) = \begin{pmatrix} \mathcal{F}_{t1}(W_t) \\ \mathcal{F}_{t2}(W_t) \end{pmatrix} \quad , \quad \mathcal{R}_t(W_t) = \begin{pmatrix} \mathcal{R}_{t1}(W_t) \\ \mathcal{R}_{t2}(W_t) \end{pmatrix}$$

where

$$\mathcal{F}_{t1}(W_t) = \begin{pmatrix} \rho v_1 k \\ \rho v_1 \varepsilon \end{pmatrix} \quad , \quad \mathcal{F}_{t2}(W_t) = \begin{pmatrix} \rho v_2 k \\ \rho v_2 \varepsilon \end{pmatrix}$$

$$\mathcal{R}_{t1}(W_t) = \begin{pmatrix} \left(\frac{\mu}{Re} + \frac{1}{\sigma_k R_t}\right) \frac{\partial k}{\partial x_1} \\ \left(\frac{\mu}{Re} + \frac{1}{\sigma_\varepsilon R_t}\right) \frac{\partial \varepsilon}{\partial x_1} \end{pmatrix}$$

$$\mathcal{R}_{t2}(W_t) = \begin{pmatrix} \left(\frac{\mu}{Re} + \frac{1}{\sigma_k R_t}\right) \frac{\partial k}{\partial x_2} \\ \left(\frac{\mu}{Re} + \frac{1}{\sigma_\varepsilon R_t}\right) \frac{\partial \varepsilon}{\partial x_2} \end{pmatrix}$$

$$\Omega(W_t) = \begin{pmatrix} -\rho\varepsilon + \mathcal{P} \\ -c_{\varepsilon_2}\frac{\rho\varepsilon^2}{k} + c_{\varepsilon_1}\frac{\varepsilon}{k}\mathcal{P} \end{pmatrix}$$

ε is the turbulence dissipation rate, and $\mathcal{P}$ is the turbulent energy production term given by

$$\mathcal{P} = -\frac{2}{3}\rho k \nabla.v + \frac{1}{R_t}\left[-\frac{2}{3}(\nabla.v)^2 + \sum_{i,j=1,2}\left[\left(\frac{\partial v_i}{\partial x_j}\right)^2 + \frac{\partial v_i}{\partial x_j}\frac{\partial v_j}{\partial x_i}\right]\right]$$

The turbulent Reynolds number R_t is obtained from the eddy viscosity μ_t

$$\frac{1}{R_t} = \mu_t = c_\mu \frac{\rho k^2}{\varepsilon}$$

and the closure coefficients σ_k, σ_ε, $c_{\varepsilon 1}$, $c_{\varepsilon 2}$, and c_μ are set to

$$\sigma_k = 1.0 \quad \sigma_\varepsilon = 1.3 \quad c_{\varepsilon 1} = 1.44 \quad c_{\varepsilon 2} = 1.92 \quad c_\mu = 0.09$$

2.3. *Wall law*

Throughout this paper, the flow domain is extended only up to a wall boundary located at a distance δ from the surface of the obstacle. A point on this wall boundary can fall within the viscous, buffer, or turbulent sublayer. The nonlinear Reichardt wall law is employed with the generalized boundary condition for the k and ε variables proposed by Jaeger and Dhatt [11] to determine the flow and turbulence unknowns on the wall boundary, which allows positioning the wall boundary closer to the obstacle. More specifically, the wall boundary conditions are set as follows

- a slip condition is imposed on the flow velocity field

  $$v.n = \dot{x}.n$$

  Here, n denotes the normal to the wall at a given point and $\dot{x}$ denotes the fluid mesh velocity vector.

- in the evaluation of the viscous flux, the wall shear stress is computed as

  $$\tau_w = \rho u_f^2$$

  and the friction velocity u_f is determined from the ALE form of Reichardt's law

  $$(v.n^\perp - \dot{x}.n^\perp)_{|_\delta} = u_f \left[2.5 \log(1 + \kappa\delta^+) + 7.8 \left(1 - e^{-\frac{\delta^+}{11}} - \frac{\delta^+}{11} e^{-0.33\delta^+} \right) \right];$$

  $\kappa = 0.41$
  where $n^\perp$ denotes the tangent to the wall boundary at a given point, and $\delta^+ = Re \dfrac{\rho\delta u_f}{\mu}$ the nondimensional wall distance.

- after the above nonlinear equation is solved for u_f, the turbulence variables k and ε are determined as follows

  $$\text{if } \delta^+ > 10 \quad k_{|_\delta} = \frac{u_f^2}{\sqrt{c_\mu}}$$

  $$\varepsilon_{|_\delta} = \frac{u_f^3}{\kappa\delta}$$

  $$\text{if } \delta^+ < 10 \quad k_{|_\delta} = \frac{u_f^2}{\sqrt{c_\mu}} \left(\frac{\delta^+}{10} \right)^2$$

  $$\varepsilon_{|_\delta} = Re \frac{{u_f}^4}{10\kappa\nu} \left[\left(\frac{\delta^+}{10} \right)^2 + \frac{2\kappa}{10\sqrt{c_\mu}} \left(1 - \left(\frac{\delta^+}{10} \right)^2 \right) \right]$$

  where $\nu = \frac{\mu}{\rho}$ is the kinematic viscosity.

3. Semidiscretization

Next, we specify the semidiscretization of the averaged Navier-Stokes and turbulence equations on an instantaneous mesh configuration.

3.1. *Spatial discretization of the averaged Navier-Stokes equations*

The spatial discretization of the averaged Navier-Stokes equations is carried out here on a triangulation of $\mathcal{D}(t)$ (or a tetrahedral mesh for three-dimensional problems) from which a dual mesh defined by control volumes or cells $C_i(t)$ is derived (Fig. 1). For each reference cell $C_i(0)$ attached to vertex i and defined in the ξ space, we introduce the characteristic function

$$\psi_i(x) = \begin{cases} 1 & \text{if } x \in C_i(0) \\ 0 & \text{otherwise} \end{cases}$$

Let $\mathcal{X}_i$ denote a generic test function associated with vertex i, and φ_i a generic finite element shape function associated with vertex i; φ_i is nonzero on all the triangles $\mathcal{T}(0)$ attached to vertex i. Eq. (2) can be transformed into

$$\int_{\mathcal{D}(0)} \frac{\partial JW}{\partial t}|_\xi \mathcal{X}_i dD_\xi + \int_{\mathcal{D}(0)} \nabla_x.\mathcal{F}^c(W,\dot{x})\mathcal{X}_i J dD_\xi = \int_{\mathcal{D}(0)} \nabla_x.\mathcal{R}(W)\mathcal{X}_i J dD_\xi \tag{4}$$

Setting $\mathcal{X}_i = \psi_i$ in the left hand side and $\mathcal{X}_i = \varphi_i$ in the right hand side of Eq. (4) leads to a mass-lumped variational form [12] of Eq. (2) that can be written as

$$\begin{aligned} \int_{C_i(0)} \frac{\partial JW}{\partial t}|_\xi dD_\xi + \int_{C_i(0)} \nabla_x.\mathcal{F}^c(W,\dot{x}) J dD_\xi = \\ \sum_{\mathcal{T}(0), i\in\mathcal{T}(0)} \int_{\mathcal{T}(0)} \nabla_x.\mathcal{R}(W)\varphi_i J dD_\xi \end{aligned} \tag{5}$$

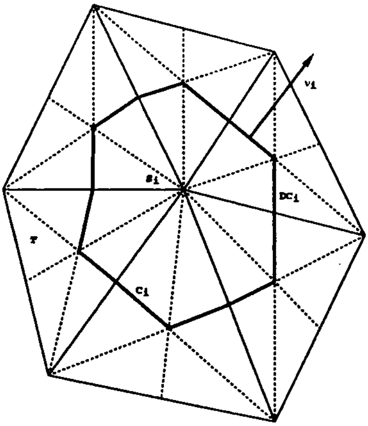

FIG. 1 – *Control volume in two dimensions*

The partial time derivative being evaluated at a constant ξ, it can be moved outside the integral sign to obtain

$$\frac{d}{dt}\int_{C_i(0)} WJdD_\xi + \int_{C_i(0)} \nabla_x.\mathcal{F}^c(W,\dot{x})JdD_\xi = \sum_{\mathcal{T}(0),i\in\mathcal{T}(0)} \int_{\mathcal{T}(0)} \nabla_x.\mathcal{R}(W)\varphi_i JdD_\xi \tag{6}$$

Switching from the ξ reference space to the x space at time t transforms Eq. (6) into

$$\frac{d}{dt}\int_{C_i(t)} WdD_x + \int_{C_i(t)} \nabla_x.\mathcal{F}^c(W,\dot{x})dD_x = \sum_{\mathcal{T}(t),i\in\mathcal{T}(t)} \int_{\mathcal{T}(t)} \nabla_x.\mathcal{R}(W)\varphi_i dD_x \tag{7}$$

Finally, integrating by parts the convective and diffusive fluxes leads to

$$\frac{d}{dt}\int_{C_i(t)} WdD_x + \int_{\partial C_i(t)} \mathcal{F}^c(W,\dot{x}).nd\sigma = -\sum_{\mathcal{T}(t),i\in\mathcal{T}(t)} \int_{\mathcal{T}(t)} \mathcal{R}(W).\nabla\varphi_i dD_x + \int_{\Gamma(t)} \mathcal{R}(W).n\varphi_i d\sigma \tag{8}$$

where n denotes now the normal to the cell boundary $\partial C_i(t)$.

3.1.1. *Approximation of the ALE convective fluxes*

Let $V(i)$, Γ_∞, and W_∞ denote the set of vertices connected to vertex i, the far-field boundary, and the value of the fluid state vector at that boundary, respectively. We approximate the ALE convective fluxes by an unstructured finite volume method as follows

$$\int_{\partial C_i(t)} \mathcal{F}^c(W,\dot{x}).n d\sigma = \sum_{j\in V(i)} \Phi^{Roe}(\mathrm{W}_i, \mathrm{W}_j, n_{ij}, \sigma_{ij}) + \Phi^{SW}_{\Gamma_\infty}(\mathrm{W}_i, \mathrm{W}_\infty, n_{i\infty}, \sigma_{i\infty}) \qquad (9)$$

where Φ^{Roe} and Φ^{SW} denote the numerical fluxes of Roe [13] and Steger-Warming [14], respectively, and n_{ij}, $n_{i\infty}$, σ_{ij}, and $\sigma_{i\infty}$ are given by

$$n_{ij} = \int_{\partial C_i(t)\cap C_j(t)} n d\sigma, \quad \sigma_{ij} = \frac{1}{\|n_{ij}\|} \int_{\partial C_i(t)\cap C_j(t)} \dot{x}.n d\sigma$$

$$n_{i\infty} = \int_{\partial C_i(t)\cap \Gamma_\infty} n d\sigma, \quad \sigma_{i\infty} = \frac{1}{\|n_{i\infty}\|} \int_{\partial C_i(t)\cap \Gamma_\infty} \dot{x}.n d\sigma$$

Roe's numerical flux is only first-order space accurate and can be written as

$$\begin{aligned}\Phi^{Roe}(U,V,\nu,\sigma) = \frac{1}{2}\,&[\mathcal{F}(U).\nu - \sigma\|\nu\|U + \mathcal{F}(V).\nu - \sigma\|\nu\|V] \\ &- \left|\mathcal{A}_W(\widetilde{W},\nu) - \sigma\|\nu\|I_d\right| \left(\frac{V-U}{2}\right)\end{aligned} \qquad (10)$$

where $\widetilde{W}$ is some mean value of U and V, $\mathcal{A}_W = \frac{\partial F}{\partial W}$, $\mathcal{A}_w = \mathcal{A}_W^+ + \mathcal{A}_W^-$, and $|\mathcal{A}_W| = \mathcal{A}_W^+ - \mathcal{A}_W^-$.

To achieve second-order accuracy, we employ a piecewise linear interpolation method that follows the principle of the MUSCL (Monotonic Upwind Scheme for Conservative Laws) procedure [15, 16]. More specifically, at the interface between two control volumes $C_i(t)$ and $C_j(t)$, we construct two intermediate fluid state vectors

$$\mathrm{W}_{ij} = \mathrm{W}_i + \frac{1}{2}(\nabla\mathrm{W})_i.(\mathrm{x}_j - \mathrm{x}_i), \quad \mathrm{W}_{ji} = \mathrm{W}_j - \frac{1}{2}(\nabla\mathrm{W})_j.(\mathrm{x}_j - \mathrm{x}_i)\,. \qquad (11)$$

and evaluate Roe's numerical flux at these two interpolated values of W

$$\Phi^{Roe}(\mathrm{W}_{ij}, \mathrm{W}_{ji}, n_{ij}, \sigma_{ij})$$

In order to reduce numerical dissipation, we compute the nodal gradients $(\nabla\mathrm{W})_i$ and $(\nabla\mathrm{W})_j$ using the following β-scheme [12]

$$(\nabla\mathrm{W})_i^\beta = (1-\beta)(\nabla\mathrm{W})_i^{Cent} + \beta(\nabla\mathrm{W})_i^{Upw} \qquad (12)$$

where $(\nabla\mathrm{W})_i^{Cent}$ is the centered gradient defined by

$$(\nabla\mathrm{W})_i^{Cent}.(\mathrm{x}_j - \mathrm{x}_i) = \mathrm{W}_j - \mathrm{W}_i$$

$(\nabla\mathrm{W})_i^{Upw}$ is the upwind gradient given by

$$(\nabla\mathrm{W})_i^{Upw} = 2(\nabla\mathrm{W})_i^{\beta=\frac{1}{2}} - (\nabla\mathrm{W})_i^{Cent}$$

and $(\nabla \mathrm{W})_i^{\beta=\frac{1}{2}}$ is the nodal gradient approximated by a Galerkin method with P_1 shape functions φ_k defined at each vertex k of a triangle $\mathcal{T}$

$$(\nabla \mathrm{W})_i^{\beta=\frac{1}{2}} = \frac{\int_{C_i(t)} \nabla \mathrm{W}_{|\mathcal{T}} dD_x}{\int_{C_i(t)} dD_x} = \frac{1}{\mathrm{Area}(C_i(t))} \sum_{\mathcal{T}, i \in \mathcal{T}} \frac{\mathrm{Area}(\mathcal{T})}{3} \sum_{k=1, k \in \mathcal{T}}^{3} \mathrm{W}_k \nabla \varphi_{k|\mathcal{T}} \tag{13}$$

Finally, in order to damp or eliminate the spurious oscillations that may occur in the vicinity of discontinuities, we employ a slope limitation algorithm that can be summarized as follows. At each interface between two control volumes, two fictitious state vectors are computed using the following interpolation scheme

$$\begin{aligned} \mathrm{W}_{ij}^{*} &= \mathrm{W}_i - 2(\nabla W)_i.(\mathrm{x}_j - \mathrm{x}_i) + (\mathrm{W}_j - \mathrm{W}_i) \\ \mathrm{W}_{ji}^{*} &= \mathrm{W}_j - 2(\nabla W)_j.(\mathrm{x}_j - \mathrm{x}_i) - (\mathrm{W}_j - \mathrm{W}_i) \end{aligned}$$

and two corresponding slopes are computed using the van Albada averaging procedure [17]

$$\begin{aligned} d\mathrm{W}_{ij} &= Ave(\mathrm{W}_j - \mathrm{W}_i, \mathrm{W}_i - \mathrm{W}_{ij}^{*}) \\ d\mathrm{W}_{ji} &= Ave(\mathrm{W}_i - \mathrm{W}_j, \mathrm{W}_j - \mathrm{W}_{ji}^{*}) \end{aligned}$$

where

$$Ave(a,b) = \begin{cases} \dfrac{a(b^2+\varepsilon^2) + b(a^2+\varepsilon^2)}{a^2+b^2+\varepsilon^2} & \text{if } a.b > 0 \\ 0 & \text{otherwise} \end{cases}$$

Then, the flux function $\Phi^{Roe}(\mathrm{W}_{ij}, \mathrm{W}_{ji}, n_{ij}, \sigma_{ij})$ is evaluated at

$$\begin{aligned} \mathrm{W}_{ij} &= \mathrm{W}_i + \frac{1}{2} d\mathrm{W}_{ij} \\ \mathrm{W}_{ji} &= \mathrm{W}_j + \frac{1}{2} d\mathrm{W}_{ji} \end{aligned}$$

It is well-known that upwind approximations of compressible flows suffer from accuracy problems in the low-Mach number limit. However, it is also known that preconditioning is a successful strategy for overcoming the numerical difficulties encountered by compressible flow solvers in the low-speed limit [18]. Hence, for low-Mach flow problems, we replace the ALE version of Roe's flux by the following ALE version of the Roe-Turkel flux

$$\begin{aligned} \Phi^{Roe-Turkel}(U,V,\nu,\sigma) = {} & \frac{1}{2}\left[\mathcal{F}(U).\nu - \sigma\|\nu\|U + \mathcal{F}(V).\nu - \sigma\|\nu\|V\right] \\ & - P^{-1}\left|P(A_W(\widetilde{W},\nu) - \sigma\|\nu\|I_d)\right|\left(\frac{V-U}{2}\right) \end{aligned} \tag{14}$$

where P is the preconditioner proposed by Turkel [18].

3.1.2. *Approximation of the diffusive fluxes*

We approximate the diffusive fluxes by a Galerkin method using P_1 shape functions φ_i. We neglect the effect of these diffusive fluxes on the far-field, and evaluate the right hand side of Eq. (8) as follows

$$\sum_{\mathcal{T}(t),i\in\mathcal{T}(t)} \int_{\mathcal{T}(t)} \mathcal{R}(W).\nabla\varphi_i dD_x = \sum_{\mathcal{T}(t),i\in\mathcal{T}(t)} \text{Area}(\mathcal{T})\mathcal{R}(\mathcal{T}).\nabla\varphi_{i|_{\mathcal{T}}} \tag{15}$$

where $\mathcal{R}(\mathcal{T})$ denotes the constant value of $\mathcal{R}$ on $\mathcal{T}$.

3.1.3. *Governing semidiscrete Navier-Stokes equations*

In summary, after the convective fluxes are discretized by the second-order finite volume method described in Section 3.1.1., and the diffusive fluxes by P_1 finite elements, the governing semidiscrete Navier-Stokes equations become

$$\frac{d}{dt}(\text{A}_i\text{W}_i) + F_i(\text{W},\text{x},\dot{\text{x}}) = R_i(\text{W},\text{x}) \tag{16}$$

where $\text{A}_i = \int_{C_i(t)} dD_x$, W_i denotes the average value of the fluid state vector over the cell $C_i(t)$, x is the vector of time-dependent grid point positions, F_i and R_i denote respectively the semidiscrete ALE convective and diffusive fluxes, and W denotes now the vector formed by the collection of the W_is.

3.2. *Spatial discretization of the turbulence equations*

Except for the presence of the term $J\Omega(W_t)$, Eq. (3) governing the k-ε turbulence model is similar to Eq. (2) governing the averaged Navier-Stokes flow. Only the two vectors W_t and W are different. Hence, the finite volume and finite element semidiscretization methods discussed in the previous sections can be equally applied to Eq. (3).

Following the same procedure outlined in Section 3.1., we first transform Eq. (3)into

$$\begin{aligned}\frac{d}{dt}\int_{C_i(t)} W_t dD_x + \int_{\partial C_i(t)} \mathcal{F}_t^c(W_t,\dot{x}).nd\sigma = &- \sum_{\mathcal{T}(t),i\in\mathcal{T}(t)} \int_{\mathcal{T}(t)} \mathcal{R}_t(W_t).\nabla\varphi_i dD_x \\ &+ \int_{\Gamma(t)} \mathcal{R}_t(W_t).n\varphi_i d\sigma + \sum_{\mathcal{T}(t),i\in\mathcal{T}(t)} \int_{\mathcal{T}(t)} \Omega(W_t)\varphi_i dD_x\end{aligned} \tag{17}$$

Next, we summarize the semidiscretization of the above equation.

3.2.1. *Approximation of the turbulence convective terms*

It is important to note that the specific semidiscretization of the turbulence equation must be such that the quantities ρk and $\rho\varepsilon$ remain positive. Therefore, we adopt Larrouturou's positivity preserving multicomponent Riemann flux function [19] to approximate the convective term in Eq. (17)

$$\begin{aligned}&\int_{\partial C_i(t)} \mathcal{F}_t^c(W_t,\dot{x}).n d\sigma = \\ &\sum_{j\in V(i)} \Phi^{Larr}(\mathrm{W}_{ti},\mathrm{W}_{tj},n_{ij},\sigma_{ij}) + \Phi^{Larr}(\mathrm{W}_{ti},\mathrm{W}_{t\infty},n_{i\infty},\sigma_{i\infty})\end{aligned} \qquad (18)$$

where n_{ij}, $n_{i\infty}$, σ_{ij} and $\sigma_{i\infty}$ have been defined in Section 3.1.1., and Φ^{Larr} is defined by [19]

$$\Phi^{Larr}(\mathrm{W}_{ti},\mathrm{W}_{tj},n_{ij},\sigma_{ij}) = \begin{pmatrix} \max(\Phi_{ij}^{Roe^\rho},0)\cdot k_i + \min(\Phi_{ij}^{Roe^\rho},0)\cdot k_j \\ \max(\Phi_{ij}^{Roe^\rho},0)\cdot \varepsilon_i + \min(\Phi_{ij}^{Roe^\rho},0)\cdot \varepsilon_j \end{pmatrix}$$

Here, $\Phi_{ij}^{Roe^\rho}$ denotes the component of Roe's numerical flux that approximates the ALE convective flux of the density across $\partial C_i(t) \cap \partial C_j(t)$. The extension of this approximation to second-order accuracy and the corresponding limitation procedure are similar to those discussed in Section 3.1.1.

3.2.2. *Approximation of the turbulence diffusive and source terms*

As for the case of the averaged Navier-Stokes equations, we approximate the diffusive fluxes of the turbulence equations — and the source term — by piecewise linear finite elements

$$\sum_{\mathcal{T}(t),i\in\mathcal{T}(t)} \int_{\mathcal{T}(t)} \mathcal{R}_t(W_t).\nabla\varphi_i dD_x = \sum_{\mathcal{T}(t),i\in\mathcal{T}(t)} \mathrm{Area}(\mathcal{T})\mathcal{R}_t(\mathcal{T}).\nabla\varphi_{i|_\mathcal{T}} \qquad (19)$$

$$\sum_{\mathcal{T}(t),i\in\mathcal{T}(t)} \int_{\mathcal{T}(t)} \Omega(W_t)\varphi_i dD_x = \sum_{\mathcal{T}(t),i\in\mathcal{T}(t)} \frac{\mathrm{Area}(\mathcal{T})}{3}\Omega(\mathcal{T}) \qquad (20)$$

where $\mathcal{R}_t(\mathcal{T})$ and $\Omega(\mathcal{T})$ denote the constant values on $\mathcal{T}$ of $\mathcal{R}_t$ and Ω, respectively.

3.2.3. *Governing semidiscrete turbulence equations*

It follows that the semidiscrete version of Eq. (17) can be written as

$$\frac{d}{dt}(\mathrm{A}_i\mathrm{W}_{ti}) + F_{ti}(\mathrm{W}_t,\mathrm{x},\dot{\mathrm{x}}) = R_{ti}(\mathrm{W}_t,\mathrm{x}) + \Omega_i(\mathrm{W}_t,\mathrm{x}) \qquad (21)$$

where $A_i = \int_{C_i(t)} d\Omega_x$, W_t is the vector formed by the collection of W_{ti}, x is the vector of time-dependent grid point positions, F_{ti} and R_{ti} are the semidiscrete ALE convective and diffusive turbulence fluxes, respectively, and Ω_i is the semidiscrete turbulence source term.

4. Time-discretization

The efficient time-discretization of Eqs. (2,3) is more challenging than that of conventional computational fluid dynamics (CFD) problems, because these ALE equations involve dynamic meshes. In particular, it was shown in [20] that a straightforward extension to moving grids of a time-integration algorithm originally developed for the solution of CFD problems on fixed grids does not in general preserve the order of time-accuracy of this algorithm. Next, we address this specific issue and specify our time-integration algorithms.

Our objective is the design of a second-order time-accurate implicit scheme because the dynamics of the boundaries of the flow problems we are interested in solving are dominated by low frequencies, and therefore it should be possible to solve these unsteady problems efficiently using relatively large time-steps.

4.1. *Time-integration of the semidiscrete averaged Navier-Stokes equations*

Let t^n and $\Delta t^n = t^{n+1} - t^n$ denote the n-th time-station and the $(n+1)$-th time-step, respectively. Integrating Eq. (16) between t^n and t^{n+1} leads to

$$\int_{t^n}^{t^{n+1}} \frac{d}{dt}(A_i W_i)dt + \int_{t^n}^{t^{n+1}} F_i(W, x, \dot{x})dt \; = \; \int_{t^n}^{t^{n+1}} R_i(W, x)dt \qquad (22)$$

The proper evaluation of the integral $\int_{t^n}^{t^{n+1}} F_i(W, x, \dot{x})dt$ raises the question of where to integrate the convective fluxes: on the mesh configuration at (t^n, x^n), on that at (t^{n+1}, x^{n+1}), in between these two configurations, outside these two configurations, or on a combination of all of these configurations? Similar questions arise as to the evaluation of $\int_{t^n}^{t^{n+1}} R_i(W, x)dt$ and the computation of the mesh velocity vector $\dot{x}$. For small time-steps, it does not matter in practice on which mesh configuration the fluxes are computed, because the differences between these configurations are not significant. However, for the desired large time-steps, the proper evaluation of the integrals $\int_{t^n}^{t^{n+1}} F_i(W, x, \dot{x})dt$ and $\int_{t^n}^{t^{n+1}} R_i(W, x)dt$ has a dramatic effect on accuracy. This specific issue has been addressed in [21, 22] for first-order time-accurate schemes, and more recently in [20] for second-order time-accurate algorithms. Here, we summarize the approach and major findings presented in [22, 20], and specify the second-order time-integration algorithm adopted in this paper.

A second-order time-accurate implicit algorithm that is popular in CFD is the second-order backward difference scheme. A generalization of this algorithm for dynamic meshes that addresses the questions raised above can be written as

$$\alpha_{n+1}\mathrm{A}_i(x^{n+1})\mathrm{W}_i^{n+1} + \alpha_n\mathrm{A}_i(x^n)\mathrm{W}_i^n + \alpha_{n-1}\mathrm{A}_i(x^{n-1})\mathrm{W}_i^{n-1} + \Delta t^n\Psi_i(\mathrm{W}^{n+1}, x^{n-l}, ..., x^n, ..., x^{n+m}, \dot{x}^{n-j}, ..., \dot{x}^n, ..., \dot{x}^{n+k}) = 0 \tag{23}$$

where j, k, l, and m are positive integers, $x^n = x(t^n)$,

$$\alpha_{n+1} = \frac{1+2\tau}{1+\tau}, \quad \alpha_n = -1-\tau, \quad \alpha_{n-1} = \frac{\tau^2}{1+\tau}, \quad \tau = \frac{\Delta t^n}{\Delta t^{n-1}}$$

$$\Psi_i = \sum_s w_s^c F_i(\mathrm{W}^{n+1}, x^{n_s^c}, \dot{x}^{n_s^c}) - w_s^d R_i(\mathrm{W}^{n+1}, x^{n_s^d}),$$

w_s^c and w_s^d are real coefficients that satisfy $\sum_s w_s^c = 1$, $\sum_s w_s^d = 1$, and $x^{n_s^c}$, $x^{n_s^d}$, and $\dot{x}^{n_s^c}$ are some linear combinations of the mesh configurations $\{x^{n-l}, .., x^n, .., x^{n+m}\}$ and their velocities $\{\dot{x}^{n-j}, .., \dot{x}^n, .., \dot{x}^{n+k}\}$. An important issue is then the proper construction of Ψ_i so that the generalized algorithm (23) retains as much as possible second-order time-accuracy on moving grids.

It can be shown that a sufficient condition for the time-integrator (23) to be mathematically consistent — that is, to be at least first-order time-accurate — is to predict exactly the state of a uniform flow. This sufficient condition, which was formulated in [20] as a geometric conservation law (GCL), can be used to determine the coefficients w_s^c and the mesh configurations $(x^{n_s^c}, \dot{x}^{n_s^c})$. For example, it was shown in [20] that for two-dimensional problems, the time-integrator (23) equipped with the following two w_s^c coefficients and two mesh configurations $(x^{n_s^c}, \dot{x}^{n_s^c})$ satisfies the GCL and achieves high accuracy

$$\left\{\begin{array}{ll} w_1^c = \alpha_{n+1}\,; & w_2^c = -\dfrac{\alpha_{n-1}}{\tau} \\ x^{n_1^c} = \dfrac{x^{n+1}+x^n}{2}\,; & x^{n_2^c} = \dfrac{x^n+x^{n-1}}{2} \\ \dot{x}^{n_1^c} = \dfrac{x^{n+1}-x^n}{\Delta t^n}\,; & \dot{x}^{n_2^c} = \dfrac{x^n-x^{n-1}}{\Delta t^{n-1}} \end{array}\right. \tag{24}$$

and for three-dimensional problems, the proposed time-integrator equipped with the following four w_s^c coefficients and four mesh configurations $(x^{n_s^c}, \dot{x}^{n_s^c})$ satisfies the GCL and achieves high accuracy

$$\left\{\begin{array}{l} w_1^c = \frac{\alpha_{n+1}}{2};\;\; w_2^c = \frac{\alpha_{n+1}}{2};\;\; w_3^c = -\frac{\alpha_{n-1}}{2\tau};\;\; w_4^c = -\frac{\alpha_{n-1}}{2\tau} \\ d_1 = \frac{1}{2}\left(1 - \frac{1}{\sqrt{3}}\right);\;\; d_2 = \frac{1}{2}\left(1 + \frac{1}{\sqrt{3}}\right) \\ x^{n_1^c} = d_1 x^{n+1} + d_2 x^n;\;\; x^{n_2^c} = d_2 x^{n+1} + d_1 x^n;\;\; x^{n_3^c} = d_1 x^n + d_2 x^{n-1}; \\ x^{n_4^c} = d_2 x^n + d_1 x^{n-1} \\ \\ \dot{x}^{n_1^c} = \dfrac{x^{n+1} - x^n}{\Delta t^n};\;\; \dot{x}^{n_2^c} = \dfrac{x^{n+1} - x^n}{\Delta t^n};\;\; \dot{x}^{n_3^c} = \dfrac{x^n - x^{n-1}}{\Delta t^{n-1}};\;\; \dot{x}^{n_4^c} = \dfrac{x^n - x^{n-1}}{\Delta t^{n-1}} \end{array}\right. \tag{25}$$

In practice, the expression of Ψ_i can be simplified as follows. For the convective terms, instead of averaging fluxes on different mesh configurations, a single flux is computed using geometrical quantities that are averaged on the same mesh configurations as in Eq. (25) and using the same weights, which reduces the computational complexity of the flux computation phase (see [20] for more details).

The principle of conservation of the state of a uniform flow W^* cannot be used as a guideline for determining the viscous coefficients w_s^d and the corresponding mesh configurations $x^{n_s^d}$, because $R_i(W^*, x^{n_s^d}) = 0$. However, these unknowns can be determined by performing a truncation error analysis of $\int_{t^n}^{t^{n+1}} R_i(W^{n+1}, x)dt$ using a Taylor series expansion, and requiring that the quantity $\Delta t^n \sum_s w_s^d R_i(W^{n+1}, x^{n_s^d})$ approximates this integral with an error $O\ (\Delta t^3)$. In [23], the authors have shown that for both two- and three-dimensional problems

$$\int_{t^n}^{t^{n+1}} R_i(W^{n+1}, x)dt = \Delta t R_i(W^{n+1}, \frac{x^{n+1} + x^n}{2}) + O(\Delta t^3)$$

It follows that the time-integrator (23) can be used with the following w_s^d coefficient and mesh configuration $x^{n_s^c}$

$$\left\{\begin{array}{ll} w_1^d & = 1 \\ x^{n_1^d} & = \frac{x^{n+1} + x^n}{2} \end{array}\right. \tag{26}$$

In summary, we advocate here the time-integration of the semidiscrete ALE averaged Navier-Stokes equations using the algorithm (23) equipped with the w_s^d coefficient and the mesh configuration given in (26), and the w_s^c coefficients and mesh configurations $(x^{n_s^c},\ \dot{x}^{n_s^c})$ given in (24) for two-dimensional problems, and in (25) for three-dimensional ones.

4.2. *Time-integration of the semidiscrete turbulence equations*

The time-integration method described in the previous section is equally applicable to the semidiscrete ALE turbulence equations (3). The turbulence source term $\int_{t^n}^{t^{n+1}} \Omega_i(\mathrm{W}_t, \mathrm{x})dt$ can be evaluated in the same manner as $\int_{t^n}^{t^{n+1}} R_{t_i}(\mathrm{W}_t, \mathrm{x})dt$ — that is, the same manner as $\int_{t^n}^{t^{n+1}} R_i(\mathrm{W}, \mathrm{x})dt$.

5. Implicit iterative defect correction method

The time-integration methodology described in the previous sections leads at each time-step to the following set on nonlinear equations

$$\alpha_{n+1}\mathrm{A}_i^{n+1}\mathrm{W}_i^{n+1} + \alpha_n\mathrm{A}_i^n\mathrm{W}_i^n + \alpha_{n-1}\mathrm{A}_i^{n-1}\mathrm{W}_i^{n-1} + \Delta t^n\overline{\Psi}_i = 0$$

$$\alpha_{n+1}\mathrm{A}_i^{n+1}\mathrm{W}_{t_i}^{n+1} + \alpha_n\mathrm{A}_i^n\mathrm{W}_{t_i}^n + \alpha_{n-1}\mathrm{A}_i^{n-1}\mathrm{W}_{t_i}^{n-1} + \Delta t^n\overline{\Psi}_{t_i} = 0$$

where

$$\overline{\Psi}_i = [\sum_s w_s^c F_i(\mathrm{W}^{n+1}, x^{n_s^c}, \dot{x}^{n_s^c})] \; - \; R_i(\mathrm{W}^{n+1}, \frac{x^{n+1}+x^n}{2})$$

$$\overline{\Psi}_{t_i} = [\sum_s w_s^c F_{t_i}(\mathrm{W}_t^{n+1}, x^{n_s^c}, \dot{x}^{n_s^c})] \; - \; R_{t_i}(\mathrm{W}_t^{n+1}, \frac{x^{n+1}+x^n}{2}) \\ - \; \Omega_i(\mathrm{W}_t^{n+1}, \frac{x^{n+1}+x^n}{2})$$

$\mathrm{A}_i^{n+1} = \mathrm{A}_i(x^{n+1})$, $\mathrm{A}_i^n = \mathrm{A}_i(x^n)$, $\mathrm{A}_i^{n-1} = \mathrm{A}_i(x^{n-1})$, and the coefficients w_s^c and mesh configurations $(x^{n_s^c}, \dot{x}^{n_s^c})$ are given in Eq. (24) for two-dimensional problems, and Eq. (25) for three-dimensional ones.

The linearization of these equations can be written as

$$\left(\alpha_{n+1}\mathrm{A}_i^{n+1} + \Delta t^n\frac{\partial\overline{\Psi}_i}{\partial\mathrm{W}}(\mathrm{W}^n)\right)(\mathrm{W}_i^{n+1} - \mathrm{W}_i^n) = \\ - \Delta t^n\overline{\Psi}_i(\mathrm{W}^n) - \alpha_{n+1}\mathrm{A}_i^{n+1}\mathrm{W}_i^n - \alpha_n\mathrm{A}_i^n\mathrm{W}_i^n - \alpha_{n-1}\mathrm{A}_i^{n-1}\mathrm{W}_i^{n-1}$$

$$\left(\alpha_{n+1}\mathrm{A}_i^{n+1} + \Delta t^n\frac{\partial\overline{\Psi}_{t_i}}{\partial\mathrm{W}}(\mathrm{W}_t^n)\right)(\mathrm{W}_{t_i}^{n+1} - \mathrm{W}_{t_i}^n) = \\ - \Delta t^n\overline{\Psi}_{t_i}(\mathrm{W}_{t_i}^n) - \alpha_{n+1}\mathrm{A}_i^{n+1}\mathrm{W}_{t_i}^n - \alpha_n\mathrm{A}_i^n\mathrm{W}_{t_i}^n - \alpha_{n-1}\mathrm{A}_i^{n-1}\mathrm{W}_{t_i}^{n-1}$$

where, $\overline{\Psi}_i$ and $\overline{\Psi}_{t_i}$ are second-order space accurate, as discussed in Section 3. It is well-known that constructing a second-order accurate spatial discretization of the jacobians $\frac{\partial\overline{\Psi}_i}{\partial\mathrm{W}}$ and $\frac{\partial\overline{\Psi}_{t_i}}{\partial\mathrm{W}}$ is a complex task [24]. For this reason, we perform a first-order semidiscretization of these jacobians and solve the above nonlinear equations by a defect-correction (Newton-like) method [25] whose convergence properties have been analyzed in [24]. For fixed meshes, it was shown in [26] that a few iterations suffice to produce a solution that is second-order accurate both in space and time.

6. Torsional springs for viscous deforming grids

A popular method for constructing a dynamic fluid mesh is the spring analogy method [27] where the fluid grid is viewed as a quasi-static pseudo-structural discrete system. In this analogy, a fictitious *lineal* spring is attached along each edge connecting two vertices i and j of the fluid mesh, and the stiffness coefficient of this spring is chosen to be inversely proportional to the length l_{ij} of the supporting edge

$$k_{ij} \propto \frac{1}{l_{ij}} \tag{27}$$

Then, at each time-station t^n, the position of the dynamic fluid mesh is obtained from the solution of the quasi-static problem

$$\begin{aligned} \mathrm{K}_{lineal}\, \mathrm{q}^n &= 0 \\ \mathrm{q}^n &= \bar{\mathrm{q}}^n \quad \text{on } \Gamma \end{aligned}$$

where K_{lineal} is the stiffness matrix associated with the fictitious lineal springs, q^n is the current displacement vector defined by

$$\mathrm{q}_i^n = \mathrm{x}_i^n - \mathrm{x}_i^0$$

and $\bar{\mathrm{q}}$ denotes the prescribed or somehow determined displacement vector of the moving boundary Γ.

The value of k_{ij} given in Eq. (27) is motivated by the fact that if during the mesh motion two vertices tend to get closer, the lineal spring attached to the edge they belong to becomes stiffer and therefore prevents them from colliding.

For many simple configurations such as isolated airfoils and wings, the lineal spring analogy method works well, provided that the fluid mesh is not very fine, and that its motion has a relatively small amplitude. However, it has been demonstrated that this method is not failure proof [28] as for more complex geometries, or larger mesh motion amplitudes, and more specifically for viscous problems that call for fine meshes, this method often results in invalid triangulations due to grid lines crossovers. This is essentially because, by design, a tension/compression lineal spring with $k_{ij} \propto 1/l_{ij}$ prevents two vertices from colliding, but does not prevent a vertex from crossing an edge that faces it.

Recently, for two-dimensional problems, the authors of [29] have proposed to upgrade the lineal spring analogy method with torsional springs that are designed to prevent a vertex from crossing an edge that faces it. The basic idea is to attach to each vertex i, and for each triangle $\mathcal{T}_{ijk}$ connected to i and to vertices j and k, a torsional spring with a stiffness coefficient C_i^{ijk} given by

$$C_i^{ijk} = \frac{1}{1+\cos\theta_i^{ijk}} \times \frac{1}{1-\cos\theta_i^{ijk}} = \frac{1}{\sin^2\theta_i^{ijk}} = \frac{l_{ij}^2\, l_{ik}^2}{4A_{ijk}^2} \tag{28}$$

where θ_i^{ijk} is the angle between the two edges ij and ik (Fig. 2), and A_{ijk} is the area of the triangle $\mathcal{T}_{ijk}$. Because $C_i^{ijk} \to \infty$ when either $\theta_i^{ijk} \to \pi$ or $\theta_i^{ijk} \to 0$, the torsional springs attached to vertex i prevent this vertex from crossing any edge that faces it and any triangle from having a zero or negative area, and therefore prevent neighboring triangles from interpenetrating each other.

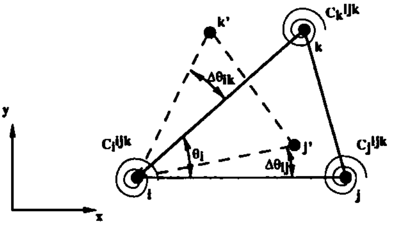

FIG. 2 – *Torsional springs for two-dimensional meshes*

Using both lineal and torsional springs, the position of the dynamic fluid mesh can be updated at each time-step by solving the following quasi-static problem

$$\begin{aligned} (\mathrm{K}_{lineal} + \mathrm{K}_{torsional})\, \mathrm{q}^n &= 0 \\ \mathrm{q}^n &= \bar{\mathrm{q}}^n \quad \text{on } \Gamma \end{aligned}$$

where $\mathrm{K}_{torsional}$ denotes the stiffness matrix associated with the fictitious torsional springs. In practice, a few iterations of a preconditioned conjugate gradient algorithm applied to the above system of equations suffice to reasonably update the dynamic mesh.

The spring analogy method equipped with both lineal and torsional springs provides an excellent mean for constructing an unstructured dynamic mesh where, at each time-step, no two vertices can collide, and no grid line crossover can occur, even under extreme deformation conditions. Furthermore, it was shown in [29] that such a strategy generates a dynamic mesh where at each time-step each triangle has as good an aspect ratio as mathematically possible; this allows a CFL(Courant-Friedrichs-Lewy)-based time-step to be kept as large as possible, which is crucial for computational performance.

In this work, we adopt the improved spring analogy method described above for generating a dynamic mesh. However, we also present a generalization of the torsional spring concept to three-dimensional unstructured meshes.

Let $\mathcal{V}_{ijkl}$ denote the tetrahedron attached to vertices i, j, k, and l, i_1 the midpoint between vertices j and k (Fig. 3), ii_1 the median of triangle $\mathcal{T}_{ijk}$ originating from vertex i, $\theta_i^{ii_1l}$ the angle between the two edges ii_1 and il, and $\theta_l^{ii_1l}$ the angle between the two edges li and li_1. Consider now triangle $\mathcal{T}_{ii_1l}$.

Two torsional springs with stiffness coefficients $C_i^{ii_1l}$ and $C_l^{ii_1l}$ determined from the two-dimensional method described above can be attached to vertices i and l. Because $C_i^{ii_1l} \to \infty$ when either $\theta_i^{ii_1l} \to \pi$ or $\theta_i^{ii_1l} \to 0$, and $C_l^{ii_1l} \to \infty$ when either $\theta_l^{ii_1l} \to \pi$ or $\theta_l^{ii_1l} \to 0$, these two torsional springs prevent vertex i from crossing the three-dimensional edge $\mathcal{T}_{jkl}$ and that edge from collapsing, and prevent vertex l from crossing the three-dimensional edge $\mathcal{T}_{ijk}$ and that edge from collapsing. Hence, by applying the two-dimensional torsional spring method to triangle $\mathcal{T}_{ii_1l}$, 4 of the collapsing mechanisms of tetrahedron $\mathcal{V}_{ijkl}$ are eliminated. Since 3 medians originating from vertex i can be constructed, 3 torsional springs based on the two-dimensional theory can be designed and attached to this vertex. Hence, using the two-dimensional approach, a total of 12 torsional springs each with a stiffness coefficient similar to that expressed in Eq. (28) can be designed and attached to vertices i, j, k, and l to prevent the volumetric collapse mechanisms of tetrahedron $\mathcal{V}_{ijkl}$. The combination of these torsional springs with the lineal springs prevents all possible collapse mechanisms of tetrahedron $\mathcal{V}_{ijkl}$.

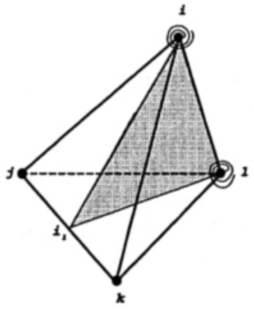

FIG. 3 – *Torsional springs for three-dimensional meshes*

7. The square cylinder benchmark problem

For vortex shedding flows such as those encountered in the buffeting analysis of aircraft and the aerodynamic stability analysis of suspension bridges, it is essential to capture correctly the Strouhal number

$$Str = \frac{fD}{V_\infty}$$

where f is the frequency of vortex shedding, D is a reference length, and V_∞ the flow free-stream velocity. Here, our objective is to assess the potential of the k-ε turbulence model for the solution of such unsteady viscous flow problems, when equipped with the wall law described in Section 2.3, and discretized by the methods presented in this paper. It should be pointed out that, a priori, the k-ε turbulence model is not designed for non-equilibrium flows. However, its popularity in the engineering community, and the important computational resources required by DNS and LES methods for high Reynolds flows are such that the investigation of the potential of this turbulence model for vortex dominated aeroelastic applications is worthwhile.

For this purpose, we consider first the two-dimensional numerical simulation of the low-speed flow past a square cylinder investigated experimentally by Lyn and by Durao, because

- this problem is representative of a large class of low-speed flows past bluff bodies, including the flow past the H section of the Tacoma Narrows Bridge investigated in Section 8. Hence, this model problem is useful for tuning some of the key parameters of our simulation methodology — such as the β parameter that controls numerical dissipation (see Eq. (12)) — for bluff body configurations.
- computational results for this problem using a variety of turbulence models are available in the literature (see for example [7]).
- a comprehensive set of experimental data is available for this flow problem [7].

The cylinder considered here has a 1 cm × 1 cm cross section. The far-field flow is assumed to be uniform. The free-stream Mach number is $M_\infty = 0.1$, and the Reynolds number is $Re = 22000$.

The two-dimensional computational domain surrounding the cross section of the cylinder is discretized into 15896 vertices (Fig. 4). The wall boundary is placed at a distance $\delta = 9 \times 10^{-3}$ from the physical surface of the obstacle. Three numerical simulations are performed on an 8-processor Silicon Graphics Origin 2000 system. In the first simulation, β (see Eq. (12)) is set to $\beta = 1/3$, because in that case the approximation of the ALE convective flux can be shown to be third-order space accurate for advection problems. In the second simulation, β is kept to $\beta = 1/3$, but the slope limiter is turned off. In the third simulation, β is set to $\beta = 1/100$ in order to minimize numerical dissipation, and the slope limiter is kept turned off. In all three simulations, the CFL number is programmed to increase from 1 to 200 during the first 10 time-steps, and is maintained at the value of 200 during all subsequent time-steps. (This corresponds to sampling the captured vortex shedding period in 36 time-steps). The calculated time histories of the lift and drag coefficients are reported in Fig. 5–6 and Fig. 7–8, respectively. A snapshot of the Mach number contours is also shown in Fig. 9 for the third simulation.

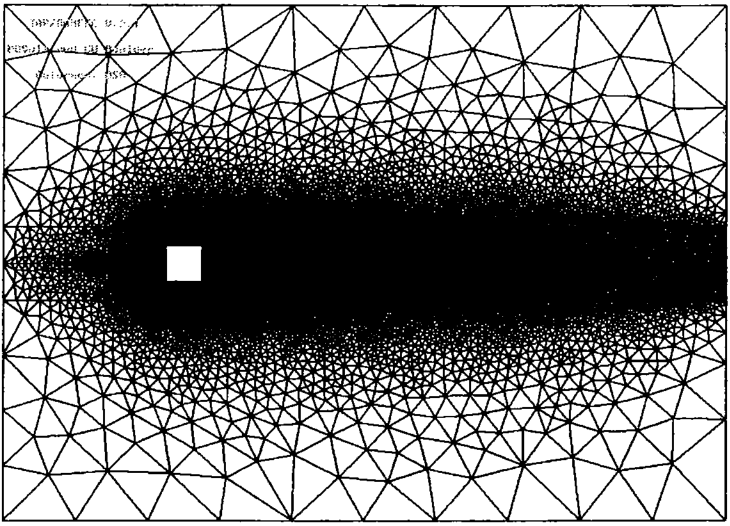

FIG. 4 – *Discretization of the computational domain*

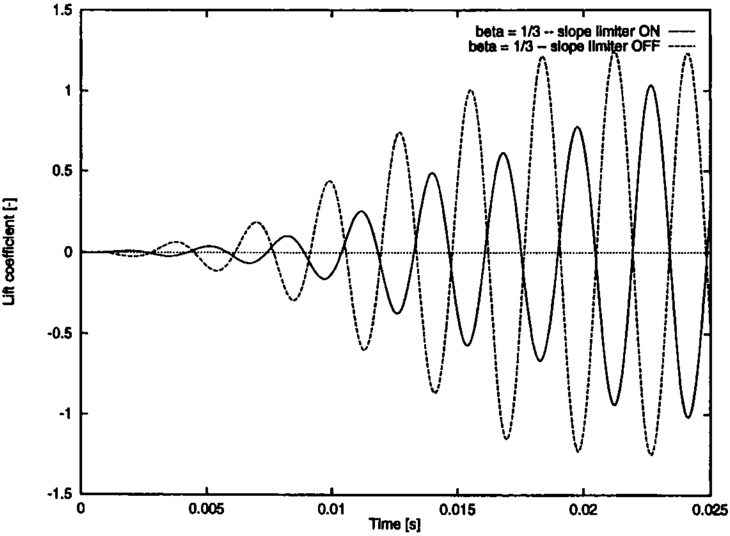

FIG. 5 – *Evolution in time of the lift coefficient* C_l ($\beta = 1/3$)

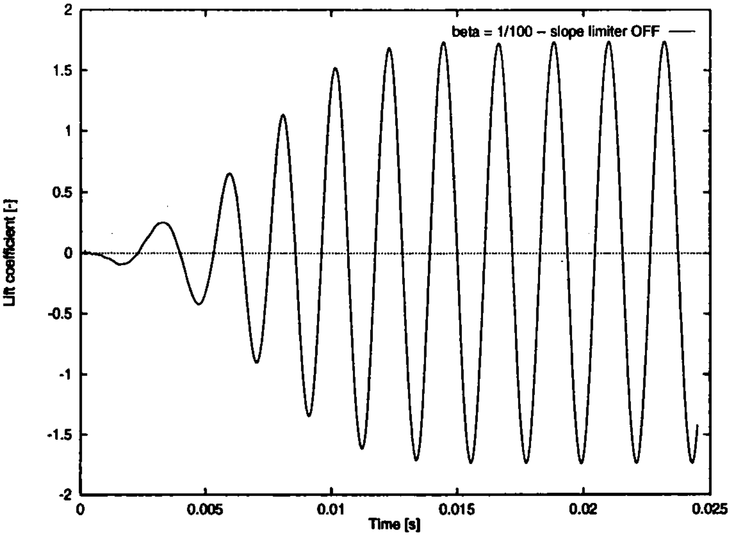

FIG. 6 – *Evolution in time of the lift coefficient C_l ($\beta = 1/100$)*

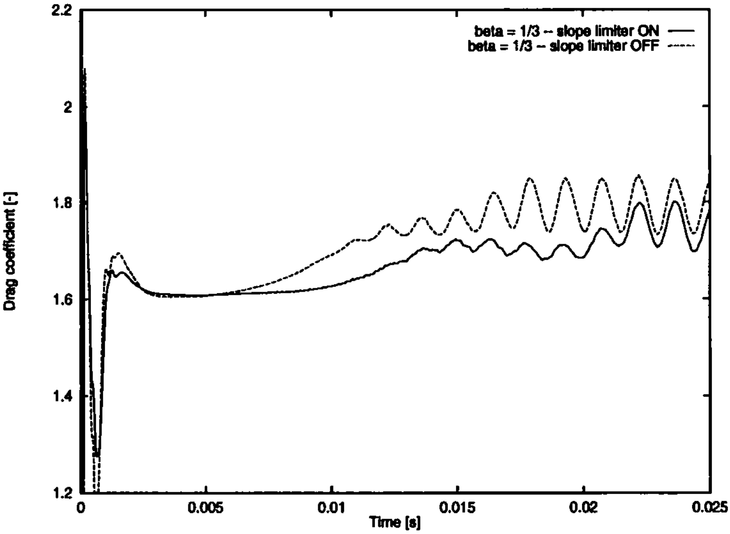

FIG. 7 – *Evolution in time of the drag coefficient C_d ($\beta = 1/3$)*

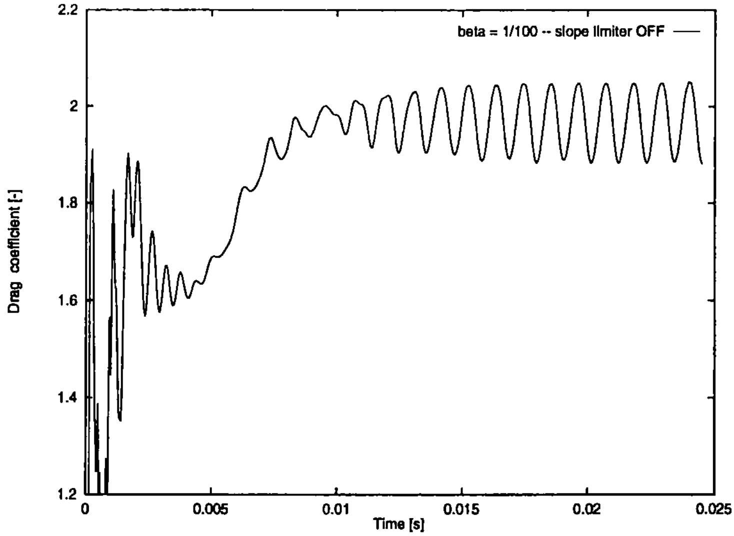

FIG. 8 – *Evolution in time of the drag coefficient* C_d ($\beta = 1/100$)

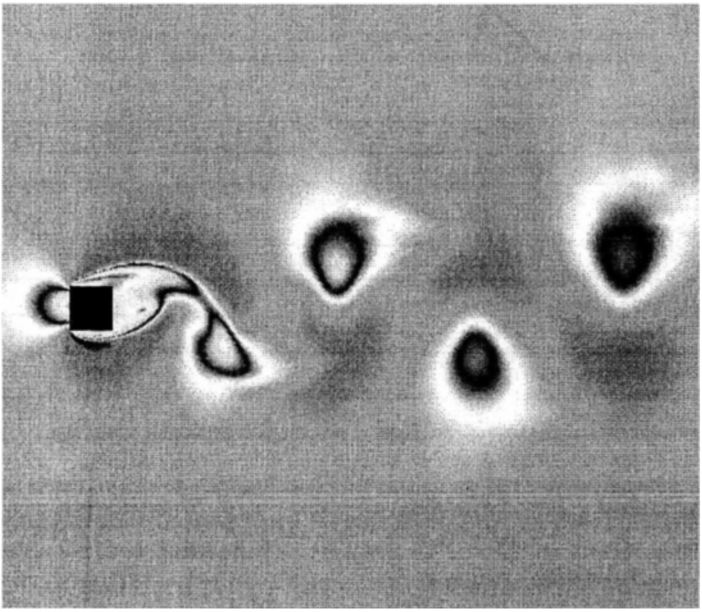

FIG. 9 – *Vortex shedding (Mach contourplot,* $\beta = 1/100$)

The reader can observe that all three simulations capture vortex shedding. However, for $\beta = 1/3$, the oscillations of the lift and drag coefficients appear to be damped, especially when the slope limiter is turned on, and their period appears to be overestimated. ¿From the lift coefficient time-histories and using a reference length $D = 0.01$ cm, we find that for the case $\beta = 1/3$ and with slope limiter, the simulated Strouhal number is $Str = 0.103$. For $\beta = 1/3$ and without slope limiter, the simulated Strouhal number is $Str = 0.104$.

For $\beta = 1/100$ and without slope limiter, the computed Strouhal number is $Str = 0.137$. This number is in excellent agreement with the experimental results of Lyn and Durao [7], and shows that the third simulation resolves correctly the vortex shedding frequency. More importantly, this result disagrees with the conclusion made in [7] — namely, that "the k-ε turbulence model combined with wall functions introduces too much damping so that no vortex shedding is predicted".

For the simulation with $\beta = 1/100$ and without slope limiter, we report in Table 1 the computed time-averaged drag coefficient $\overline{C_d}$, and computed amplitudes of the oscillations of the lift and drag coefficients $\widetilde{C_l}$ and $\widetilde{C_d}$. We contrast these results with the computational results of Franke and Rodi using a $k - \varepsilon$ and a Reynolds stress equation (RSE) turbulence models with logarithmic wall functions [7], and compare them with the experimental results of Lyn as well as those of Durao [7]. We conclude that when properly discretized in space and time, the k-ε turbulence model with Reichardt's wall law can resolve the unsteady mean of a vortex shedding flow.

Table 1. Validation of the computational results

	Franke & Rodi	Franke & Rodi	This Work	Experimental
Turb. Model	$k - \varepsilon$	RSE	$k - \varepsilon$	-
Str	stationary	0.136	0.137	Lyn 0.135 Durao 0.139
$\overline{C_d}$	1.55	2.15	1.97	2.05-2.23
$\widetilde{C_d}$	-	0.383	0.085	-
$\widetilde{C_l}$	-	2.11	1.74	-

8. Aeroelastic analysis of the Tacoma Narrows Bridge

Next, we proceed to the aerodynamic stability analysis of the Tacoma Narrows Bridge. This bridge had an H-shaped cross section that is known to give rise to vortex shedding. When the frequency of shedding vortices agrees with a natural frequency of the structure (resonance condition), the structure becomes aeroelastically unstable as its amplitude of oscillation reaches the maximum and leads to destruction. It was observed that the Tacoma Narrows Bridge failed at a critical wind speed of 42 mph (18.8 m/s) while developing a torsional oscillatory movement. The structure as built should have been able to resist a *steady* wind of at least 100 mph (44.7 m/s) if no oscillation had occurred [3].

Our objective here is to apply the simulation methodology described in the previous sections to predict numerically the (torsional) critical wind speed of the Tacoma Narrows Bridge.

8.1. *Computational models*

In most wind tunnel tests, sectional models are used for the examination of the aerodynamic stability of bridge road decks. Typically, a representative length of the deck is supported in the wind tunnel by a system of springs representing the elastic properties of the bridge. Therefore, we adopt here the two-dimensional computational structural model graphically depicted in Fig. 10. This model has two-degrees of freedom: u_y representing the bending motion of the deck, and u_θ representing its torsional motion.

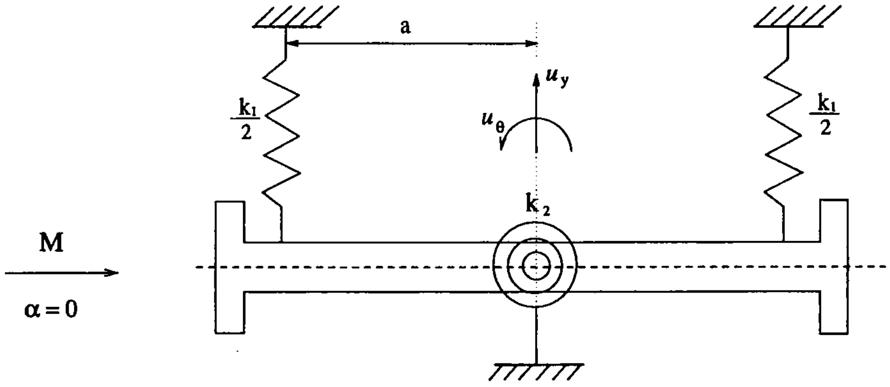

FIG. 10 – *Two-dimensional aeroelastic model of a suspension bridge*

The computational structural model described here is assumed to be undamped. Because of symmetry, the elastic center of the structure is located at its center of gravity, and its bending and torsion modes are uncoupled. Hence, the dynamic behavior of this structural model is governed by the ordinary differential equations

$$\begin{aligned} \ddot{\mathcal{U}}(t) + \Omega^2 \mathcal{U}(t) &= F(t) \\ \mathcal{U}(0) &= \mathcal{U}_0 \\ \dot{\mathcal{U}}(0) &= \dot{\mathcal{U}}_0 \end{aligned} \tag{29}$$

where a dot superscript designates a time-derivative, $\mathcal{U}_0$ and $\dot{\mathcal{U}}_0$ are the specified initial displacement and velocity vectors,

$$\Omega^2 = \begin{bmatrix} \omega_1^2 & 0 \\ 0 & \omega_2^2 \end{bmatrix} \qquad \mathcal{U}(t) = \begin{bmatrix} u_y(t) \\ u_\theta(t) \end{bmatrix} \qquad F(t) = \begin{bmatrix} l(t) \\ m(t) \end{bmatrix}$$

$$\begin{aligned}
\omega_1^2 &= k_1/m\\
\omega_2^2 &= (k_2 + k_1 a^2)/J\\
l(t) &= (\tfrac{1}{2}\rho_\infty V_\infty^2 L_\infty C_l)/m\\
m(t) &= (\tfrac{1}{2}\rho_\infty V_\infty^2 L_\infty^2 C_m)/J
\end{aligned}$$

ω_1 is the circular frequency of the bending mode, ω_2 is the circular frequency of the torsion mode, m is the mass per unit length and J the mass moment of inertia per unit length of the deck, V_∞ is the free-stream wind velocity, and L_∞ is the length of the structural model. For the Tacoma Narrows Bridge deck, reference [33] recommends the following values

$$\begin{aligned}
f_1 &= \omega_1/2\pi &&= 0.84\ \text{Hz}\\
f_2 &= \omega_2/2\pi &&= 1.11\ \text{Hz}\\
m & &&= 8500\ \text{Kg/m}\\
J & &&= 167344\ \text{Kgm}^2\text{/m}\\
L_\infty & &&= 12\ \text{m}
\end{aligned}$$

The modeling of the deck of the Tacoma Narrows Bridge as an H-shaped profile is supported by studies reported in [30]. Indeed, the authors of [30] have shown that the torsional stability of an H-shaped section is similar to that of the Tacoma Narrows deck when its depth-to-width ratio is set to that of the real bridge section (value = 0.21). The flow domain around this H-shaped obstacle is discretized by an unstructured mesh with 13232 vertices (Fig. 11).

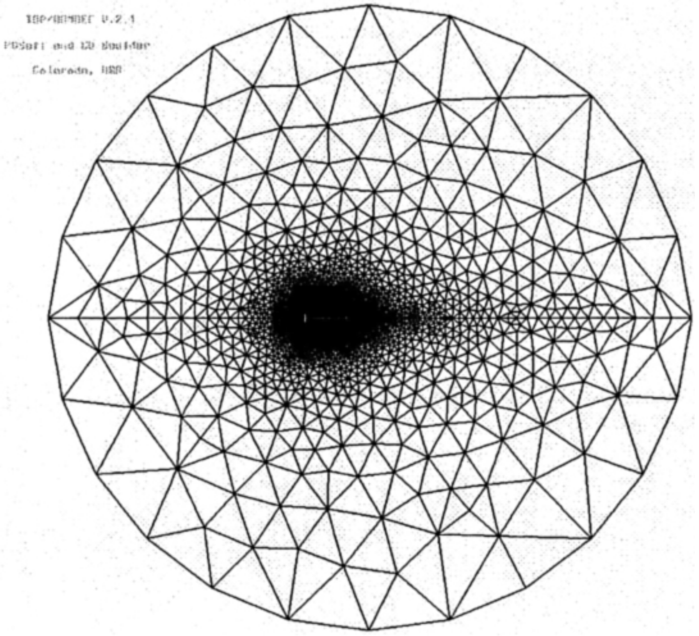

FIG. 11 – *Discretization of the computational flow domain*

We solve the coupled fluid/structure equations (Eq. (16), Eq. (21) and Eq. (29)) by a staggered procedure [31] where the time-integrator (23) is applied to the flow problem, and the trapezoidal rule [32] to the structural problem.

8.2. *Investigation of the critical wind speed*

Throughout this section, the Reynolds number is set to $Re = 10^6$, the free-stream density to $\rho_\infty = 1.293$ Kg/m^3, the free-stream pressure to $P_\infty = 101300$ Pa, and the β parameter to $\beta = 1/100$. The wall boundary is placed at a distance $\delta = 3 \times 10^{-3}$ from the physical surface of the obstacle. The slope limiter is turned off, and the time-stepping strategy employed for the square cylinder benchmark problem is also applied here (36 time-steps per vortex shedding period).

First, the structural model is frozen at a zero angle of attack, and a series of flow computations at different free-stream Mach numbers are performed to determine a value of M_∞ for which the computed vortex shedding frequency is close to that of the torsion mode of the structure $f_2 = 1.11$ Hz. It is found that at $M_\infty = 0.07$ ($V_\infty = 23.18$ m/s), the vortices shed at a frequency equal to 1.09 Hz. This suggests that $M_\infty = 0.07$ is a good approximation of the torsional critical Mach number.

Next, three aeroelastic simulations are performed with $M_\infty = 0.068$, $M_\infty = 0.070$, and $M_\infty = 0.072$. The corresponding structural vibration results are reported in Fig. 12 and Fig. 13. From the computed time-histories of the twisting angle u_θ, we conclude that the critical Mach number for torsion is $M_\infty = 0.07$, and therefore the critical wind speed is $V_\infty = 23.18$ m/s. Since the critical wind speed that was "observed" for the torsional instability was estimated at $V_\infty = 18.8$ m/s [3], it follows that our numerical simulations reproduce the observed results with a 23% relative error. Note that the computed critical wind speed strongly depends on the value of ω_2 used in the numerical simulations, and that in this work, this value was set to that recommended in [33].

From the results reported in Fig. 13, we also conclude that the deck is aeroelastically unstable in bending at $M_\infty = 0.068$ and $M_\infty = 0.070$, but becomes aeroelastically stable in bending at $M_\infty = 0.072$. Hence, our numerical simulations indicate the existence of (a) a critical Mach number ($M_\infty = 0.068$) at which the deck is aeroelastically unstable in bending but is stable in torsion, (b) a higher critical Mach number ($M_\infty = 0.07$) at which the deck becomes aeroelatically unstable in both bending and torsion, (c) an even higher critical Mach number ($M_\infty = 0.072$) at which the deck re-becomes aeroelastically stable in bending, but remains unstable in torsion. This qualitative result is in agreement with the experiments performed by Dunn on an H-shaped aeroelastic deck model and described in [3].

Finally, we display in Fig. 14 a snapshot of the shedding vortices at $M_\infty = 0.07$ when the twisting angle reaches the value $u_\theta = 3^{\text{deg}}$.

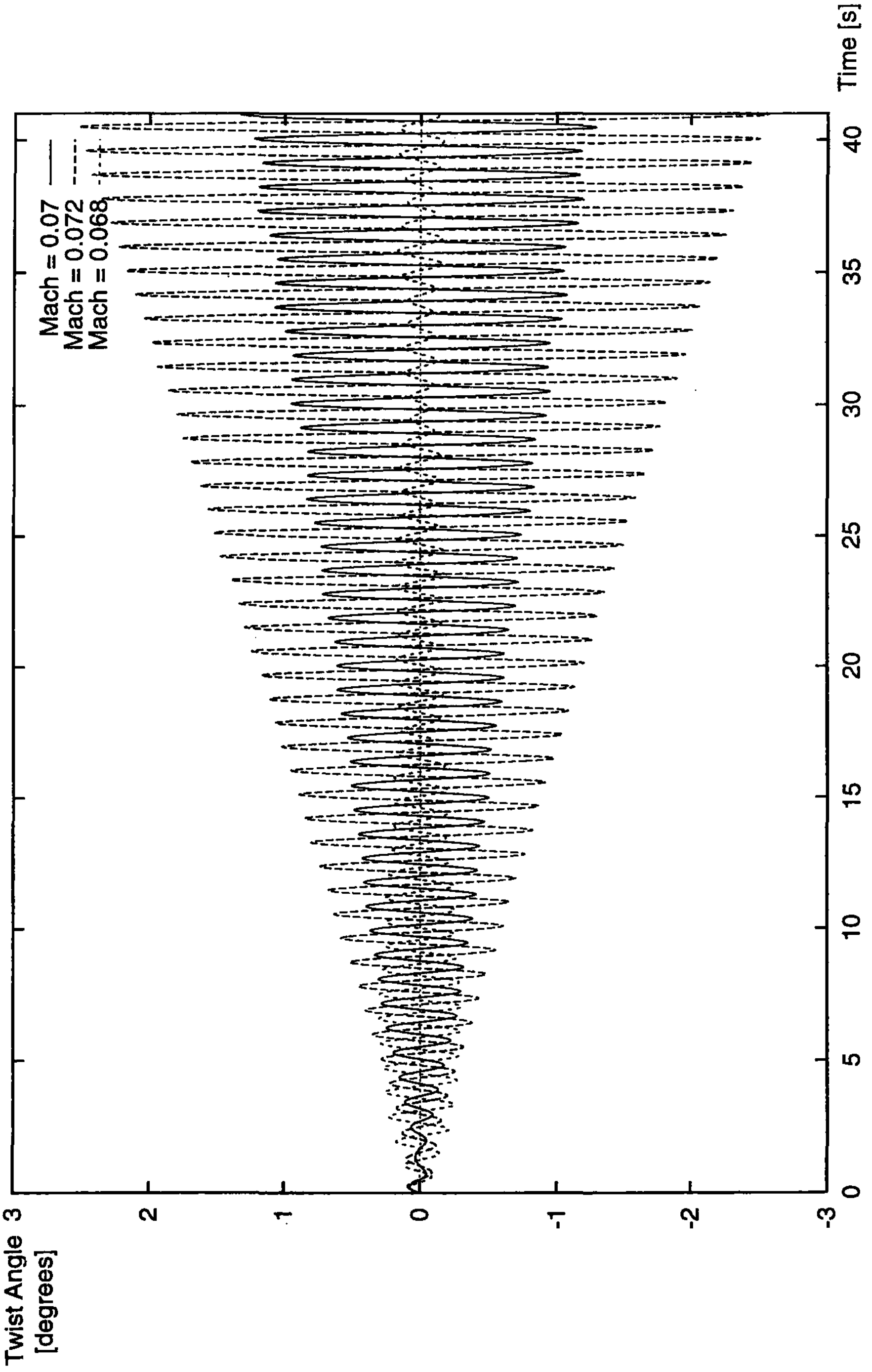

FIG. 12 – *Torsional oscillations for various free-stream Mach numbers*

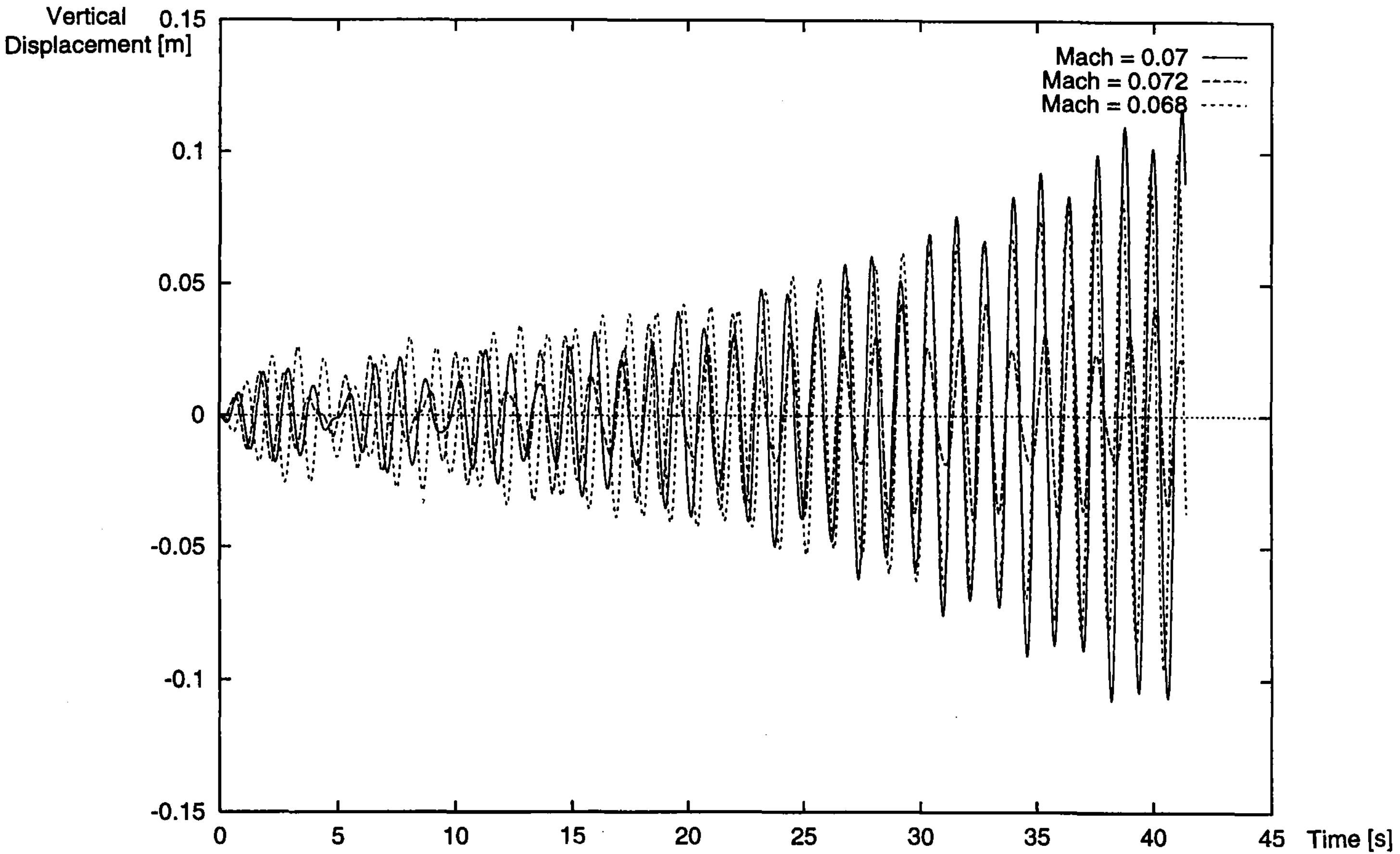

FIG. 13 – *Vertical (bending) oscillations for various free-stream Mach numbers*

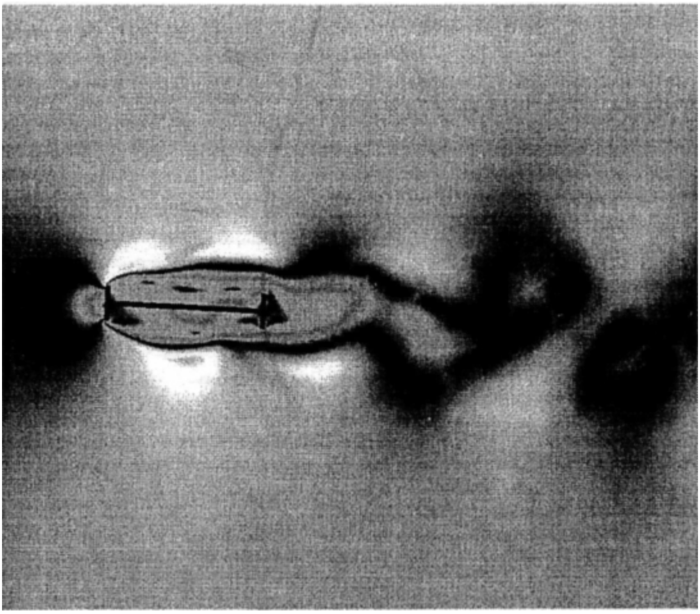

FIG. 14 – *Vortex shedding for* $M_\infty = 0.07$ *and at* $\alpha = 3^{\text{deg}}$

9. Conclusion

We have overviewed a methodology for the solution on unstructured dynamic meshes of the time-averaged Navier-Stokes equations equipped with the k-ε turbulence model and Reichardt's wall law. We have applied this methodology to the simulation of the flow past a fixed square cylinder, and the aeroelastic stability analysis of a sectional dynamic model of the Tacoma Narrows Bridge. For both low-speed high Reynolds applications, we have shown that when properly discretized, the k-ε turbulence model with Reichardt's wall law is capable of resolving the unsteady mean of the vortex shedding dominated flow.

References

[1] J. W. Edwards and J. B. Malone, *Current Status of Computational Methods for Transonic Unsteady Aerodynamics and Aeroelastic Applications*, Comput. Sys. Engrg. 1992, 3:545-569.

[2] E. Simiu and R.H Scanlan, *Wind Effects on Structures*, John Wiley & Sons, 2nd Edition, 1986.

[3] Y. C. Fung, *An Introduction to the Theory of Aeroelasticity*, Dover Publications, Inc., 1969.

[4] M. Xia and G.E. Karniadakis, *The Spectrum of the Turbulent Near-Wake: a Comparison of DNS and LES*, Proc. 1st AFOSR Int. Conference on DNS/LES, Ruston, LA, 1997.

[5] B. E. Launder and D. B. Spalding, *The Numerical Computation of Turbulent Flows*, Comput. Meths. Appl. Mech. Engrg. 1974, 3:269-289.

[6] J. Donea, *An Arbitrary Lagrangian-Eulerian Finite Element Method for Transient Fluid-Structure Interactions*, Comput. Meths. Appl. Mech. Engrg. 1982, 33: 689-723.

[7] R. Franke and W. Rodi, *Calculation of Vortex Shedding Past a Square Cylinder With Various Turbulence Models*, Eighth Symposium on Turbulent Shear Flows, Technical University of Munich, 1991.

[8] C. Farhat, M. Lesoinne and N. Maman, *Mixed Explicit/Implicit Time Integration of Coupled Aeroelastic Problems: Three-Field Formulation, Geometric Conservation and Distributed Solution*, Internat. J. Numer. Meths. Fluids 1995, 21: 807-835.

[9] T. Tezduyar, M. Behr and J. Liou, *A New Strategy for Finite Element Computations Involving Moving Boundaries and Interfaces - The Deforming Spatial Domain/Space-Time Procedure: I. The Concept and the Preliminary Numerical Tests*, Comput. Meths. Appl. Mech. Engrg. 1992, 94: 339–351.

[10] A. Masud, *A Space-Time Finite Element Method for Fluid Structure Interaction*, Ph. D. Thesis, Stanford University, 1993.

[11] M. Jaeger and G. Dhatt, *An Extended $k-\epsilon$ Finite Element Model*, Internat. J. Numer. Meths. Fluids 1992, 14:1325-1345.

[12] C. Farhat, L. Fezoui and S. Lantéri, *Two-Dimensional Viscous Flow Computations on the Connection Machine: Unstructured Meshes, Upwind Schemes, and Massively Parallel Computations*, Comput. Meths. Appl. Mech. Engrg. 1993, 102:61-88.

[13] P. L. Roe, *Approximate Reimann Solvers, Parameters Vectors and Difference Schemes*, J. Comp. Phys. 1981, 43:357–371.

[14] J. Steger and R. F. Warming, *Flux Vector Splitting for the Inviscid Gas Dynamic with Applications to Finite-Difference Methods*, J. Comp. Phys. 1981, 40:263-293.

[15] B. Van Leer, *Towards the Ultimate Conservative Difference Scheme V: a Second-Order Sequel to Godounov's Method*, J. Comp. Phys. 1979, 32:361-370.

[16] A. Dervieux, *Steady Euler Simulations Using Unstructured Meshes*, Von Kármán Institute Lecture Series, 1985.

[17] G. D. van Albada, B. van Leer and W. W. Roberts, *A Comparative Study of Computational Methods in Cosmic Gas Dynamics*, Astron. Astrophys. 1982, 108:76-84.

[18] E. Turkel, *Preconditionned Methods for Solving the Incompressible and Low-Speed Compressible Equations*, J. Comp. Phys. 1987, 72:277-298.

[19] B. Larrouturou, *How to preserve the mass fraction positivity when computing compressible multi-component flows*, J. Comp. Phys. 95, 1:59-84.

[20] B. Koobus and C. Farhat, *Second-Order Time-Accurate and Geometrically Conservative Implicit Schemes for Flow Computations on Unstructured Dynamic Meshes*, Comput. Meths. Appl. Mech. Engrg., (submitted for publication). Also published as Technical Report CU-CAS-97-12, College of Engineering, The University of Colorado at Boulder, June 1997.

[21] M. Lesoinne and C. Farhat, *Geometric Conservation Laws for Aeroelastic Computations Using Unstructured Dynamic Meshes*, AIAA Paper 95-1709, 12th AIAA Computational Fluid Dynamics Conference, San Diego, June 19-22, 1995.

[22] M. Lesoinne and C. Farhat, *Geometric Conservation Laws for Flow Problems with Moving Boundaries and Deformable Meshes, and Their Impact on Aeroelastic Computations*, Comput. Meths. Appl. Mech. Engrg. 1996, 134:71-90.

[23] B. Koobus and C. Farhat, *Time-Accurate Algorithms for the Evaluation of the Viscous Fluxes Associated with Unsteady Flows and Unstructured Moving Meshes,* AIAA Paper 96-2384, 14th AIAA Applied Aerodynamics Conference, New Orleans, Louisiana, June 18-20, 1996.

[24] J.-A Désidéri and P. W. Hemker, *Convergence Analysis of the Defect-Correction Iteration for Hyperbolic Problems,* SIAM J. Sci. Comput. 1995, 16:88-118.

[25] K. Bohmer, P. Hemker, and H. Stetter, *The Defect Correction Approach*, Comput. Supp. 1984, 5:1-32.

[26] R. Martin and H. Guillard, *A Second-Order Defect Correction Scheme for Unsteady Problems*, Comput. and Fluids 1996, 25:9-27.

[27] J. T. Batina, *Unsteady Euler Airfoil Solutions Using Unstructured Dynamic Meshes,* AIAA Paper No. 89-0115, AIAA 27th Aerospace Sciences Meeting, Reno, Nevada, January 9-12, 1989.

[28] S. R. Chakravarthy and K. Y. Szema, *Computational Fluids Dynamics Capability for Internally Carried Store Separation,* Rockwell Intl. Corp. Rep. SC-71039-TR, Science Center, Thousand Oaks, CA, 1991.

[29] C. Farhat, C. Degand, B. Koobus and M. Lesoinne, *Torsional Springs for Two-Dimensional Dynamic Unstructured Fluid Meshes,* Comput. Meths. Appl. Mech. Engrg. (submitted for publication). Also published as Technical Report CU-CAS-97-03, College of Engineering, The University of Colorado at Boulder, January 1997.

[30] R. H. Scanlan and J. J. Tomko, *Airfoil and Dridge Deck Flutter Derivatives*, J. Engrg. Mech. 1971, 97:1717-1737.

[31] S. Piperno, C. Farhat and B. Larrouturou, *Partitioned Procedures for the Transient Solution of Coupled Aeroelastic Problems - Part I: Model Problem, Theory, and Two-Dimensional Application,* Comput. Meths. Appl. Mech. Engrg. 1995, 124:79-112.

[32] T. J. R. Hughes, *The Finite Element Method*, Prentice-Hall, Inc., 1987.

[33] D. Amsler, *Etude Théorique et Expérimentale des Ponts à Câbles de Très Grande Portée: Ponts Suspendus et Ponts Hybrides*, Thèse No. 1290, Ecole Polytechnique Fédérale de Lausanne, 1994.